

Article

Efficient Dye-Sensitized Solar Cells Composed of Nanostructural ZnO Doped with Ti

Mati Ur Rahman ^{1,2}, Mingdeng Wei ^{1,2,*}, Fengyan Xie ^{1,2} and Matiullah Khan ^{3,*} 

¹ State Key Laboratory of Photocatalysis on Energy and Environment, Fuzhou University, Fuzhou 350002, China; matiurrahman617@yahoo.com (M.U.R.); asifncp@yahoo.com (F.X.)

² Institute of Advanced Energy Materials, Fuzhou University, Fuzhou 350002, China

³ Department of Physics, Kohat University of Science and Technology, Kohat 26000, Pakistan

* Correspondence: wei-mingdeng@fzu.edu.cn (M.W.); matiullahustb@gmail.com (M.K.); Tel.: +86-0591-22865057 (M.W.)

Received: 27 February 2019; Accepted: 10 March 2019; Published: 17 March 2019



Abstract: Photoanode materials with optimized particle sizes, excellent surface area and dye loading capability are preferred in good-performance dye sensitized solar cells. Herein, we report on an efficient dye-sensitized mesoporous photoanode of Ti doped zinc oxide (Ti-ZnO) through a facile hydrothermal method. The crystallinity, morphology, surface area, optical and electrochemical properties of the Ti-ZnO were investigated using X-ray photoelectron spectroscopy, transmission electron microscopy and X-ray diffraction. It was observed that Ti-ZnO nanoparticles with a high surface area of $131.85 \text{ m}^2 \text{ g}^{-1}$ and a controlled band gap, exhibited considerably increased light harvesting efficiency, dye loading capability, and achieved comparable solar cell performance at a typical nanocrystalline ZnO photoanode.

Keywords: Ti doped ZnO; dye-sensitized solar cell; bandgap energy; photovoltaic performance

1. Introduction

Environmental challenges and increasing global energy consumption demand clean and renewable energy to support the activities of modern society [1]. To convert solar energy directly into electricity using solar cells is one of the most feasible technologies. As an alternative to the conventional silicon-based solar cell, dye-sensitized solar cells (DSSCs) have attracted tremendous interest due to their simple fabrication process, low manufacturing cost, and environmentally-friendly advantages [2–6]. Thus far, an extensive study has been carried out on the TiO_2 nanoparticle as a photoelectrode since 1991 [7,8], although the TiO_2 nanoparticle showed more than 14% power conversion efficiency when used as a photoanode due to its higher surface area. However, its poor long-term stability and low electron mobility are concerns [9,10]. Excluding TiO_2 , studies on other alternative semiconductor metal oxides, such as SnO_2 , ZnO , Nb_2O_5 and Zn_2SnO_4 , have been conducted [11–19]. Among these, ZnO has received increasing interest as a promising alternative photoanode material for DSSCs due to similar electron affinities and band gap energy (E_g), i.e., 3.2 eV and 3.3 eV compared with TiO_2 , and has excellent electron diffusivity [20,21]. At the same time, ZnO is probably richer in diverse morphologies compared to any known materials [22–24]. More recently, several studies have focused on the diverse morphology and multidimensionality of TiO_2 and ZnO with regards to robust photocatalytic activity of DSSCs with increasing electron transport and higher surface-to-volume ratios [25–27]. Additionally, ZnO has amazing merits like stability against photo corrosion, low cost, large excitation binding energy (60 eV), easier synthesis, and surface modification [28]. However, the photovoltaic performance of ZnO -based dye-sensitized solar cells is still poor, which could be caused by the narrow absorption spectral range, the quick recombination

of photo-generated electron–hole pair occurring in or on the surface photoanode and the instability of film in acidic dye solution in the case of ZnO materials [29]. In principle, ZnO-based electrodes could achieve a similar or even better photovoltaic performance if the aforementioned drawbacks could be overcome. Up to now, a number of possible strategies have been adopted to tackle these issues of ZnO electrodes. The morphological surface modification with nanoparticles of noble metals (Au, Pt, Pd, Ag, etc.) has been widely employed to decorate ZnO by doping to suppress carrier recombination [30,31]. The light sensing properties can be improved by passivation of the defect in the bulk material and at the oxide interface with dangling bond fixing [32]. Considering the economic and limited sources of noble metals, in this prospective study, Ti-doped ZnO and undoped ZnO nanoparticles were fabricated using a hydrothermal route with the aim to achieve an efficient charge separation, interfacial charge transfer to adsorbed dye to increase lifetime of charge carrier, and enhancing the photovoltaic performance of ZnO-based DSSCs.

2. Materials and Methods

2.1. Synthesis of Materials

Titanium-doped zinc oxide nanoparticles were synthesized using a facile hydrothermal route. In a typical procedure, 1.25 mmol zinc acetate dihydrate was added to methanol and stirred for 20 min, then 2 mmol of potassium hydroxide (KOH) was dropped to the solution, and a calculated amount (Ti = 1, 2, 5 and 7.5 wt%) of titanium isopropoxide (TTIP) was introduced under continuous stirring. The reaction mixture was further stirred and refluxed at 60–80 °C. The transparent color of the zinc acetate solution changed to transparent white, which indicated the starting of Ti-ZnO synthesis. After several minutes of stirring, the reaction mixture was transferred into a Teflon lined autoclave and kept in oven at 180 °C for 12–15 h. After cooling to room temperature, the yellowish solution was separated by centrifugation (8000 rpm) for 10 min and washed several times with absolute ethanol. Eventually, the powder was dried in vacuum at 60 °C overnight and calcined at 500 °C for 2 h in Ar. As a reference sample, the undoped zinc oxide nanoparticles were also synthesized via the same procedure except for the addition of TTIP.

2.2. Fabrication of Dye-Sensitized Solar Cells

2.2.1. Paste Preparation

Different pastes of ZnO and titanium-doped zinc oxide (Ti-ZnO) were prepared according to previously reported literature [33,34]. Typically, ethyl cellulose, α -terpineol (10, 5% by weight) and zinc oxide or Ti-ZnO nanoparticles were suitably dispersed in ethanol using an Ultra-Turrax T25 homogenizer followed by a rotary evaporator to concentrate up to 20 wt%.

2.2.2. Films Fabrication

Photoanodes were prepared through a screen printing method with as prepared zinc oxide and Ti-ZnO paste applied on an FTO substrate (sheet resistance $8 \Omega \text{ sq}^{-1}$, Pilkington, and followed by sintering at 450 °C for 30 min.

2.2.3. Dye Loading

The dye-loading capability of the photoanodes was estimated photometrically. The ZnO and Ti doped ZnO with various percentages of photoanodes loaded with N719 dyes were immersed in 10 mM NaOH at 30 °C overnight. The most intense band intensity was the region of 550 to 515 nm of the adsorption spectrum and was used to calibrate the dye loading.

2.2.4. Device Fabrication

The Ti-ZnO and ZnO electrodes fabricated as described above were immersed in 0.5 mM solution of N719 dye in isopropyl alcohol and acetonitrile (1:1 v/v) for 2 h at 30 °C and then rinsed with acetonitrile and dried with a nitrogen gas flow. The electrolyte was composed of 0.6 M 1,2-dimethyl-3-n-propylimidazolium iodide (DMPII), 0.05 M I₂, 0.1 M LiI, in 3-methoxypropionitrile with 0.5 M 4-tertbutylpyridine (TBP). A counter electrode was fabricated via dropping of 5 mM H₂PtCl₆ on a FTO substrate and sintered at 400 °C for 30 min. Afterwards, a polyethylene spacer was sandwiched between a dye-sensitized photoanode and a Pt counter electrode to prevent the cell from short circuiting. For the last step of DSSC fabrication, the redox electrolyte was injected into the gap of the spacer. ZnO cells were fabricated for comparison of Ti-ZnO based device photovoltaic performance to a known system.

2.3. Characterization of the Materials and Measurement of the Photovoltaic Performance

The phase purity and structural properties of the materials were analyzed by powder X-ray diffraction (XRD) on a Rigaku Ultima IV X-ray diffractometer using Cu K α radiation ($\lambda = 1.5418 \text{ \AA}$). A scanning electron microscope (SEM, Hitachi S4800) was applied to determine the size and morphology, and a transmission electron microscopy (TEM) was performed on a Tecnai G2 F20 (FEI, Hillsboro, OR, USA) transmission electron microscope to further characterize the morphology and intrinsic structure of the materials. The N₂ adsorption-desorption isotherms of Ti-ZnO were performed on an ASAP 2020 surface area analyzer (Micromeritics, Norcross, GA, USA). The film thickness was measured on a profilometer (Accretch Surfcom 130A). A Shimadzu UV-2450 UV-vis spectrophotometer and a Renishaw inVia Raman microscope were used for spectroscopic measurement. The Keithley 2400 SourceMeter under simulated AM 1.5 G illumination (Pecell, with a 1000 W Xe lamp and AM 1.5 filter) was used to investigate current-voltage (I-V) characteristic. Incident photon-to-current conversion efficiency (IPCE) spectra were recorded on a PEC S-20 (Pecell, Technology Co., Ltd., Yokohama, Japan) multimeter. Electrochemical impedance spectroscopy (EIS) was conducted on the electrochemical workstation IM6 (Zahner, and a bias potential of -0.7 V in dark condition with an 80 MHz–3 kHz range.

3. Results and Discussion

The crystallographic phases of ZnO and Ti-ZnO were analyzed from X-ray diffraction patterns, as shown in Figure 1A. All of the diffraction peaks match the standard phase (JCPDS # 01-079-0207), indicating that the synthesized materials are well crystallized and phase pure hexagonal ZnO. However, slight shifting of the peaks to a higher angle was observed for titanium-containing materials, Ti(7.5%)-ZnO compared with the ZnO, which implied the inward relaxation of the lattice due to the substitution of the bigger Zn²⁺ atom (ionic radius = 0.74 Å) with smaller ion (Ti⁴⁺ ionic radius = 0.68 Å) which had larger size as ions in the crystalline structure, and caused a change in the lattice parameter value without changing the crystal structure of the ZnO lattice. The average value of crystallite size and strain estimated by the Debye-Scherrer equation, $D = K\lambda / \beta \cos\theta$ [35], and the XRD patterns of all samples are shown in Figure S2 and their physiochemical characteristics, including surface area, strain, crystallite and pore size, are summarized in Table S1.

Two small negligible peaks were found at 25 and 27 degrees with higher dopant concentrations, which may mean that trace amount of Ti was converted into TiO₂ which was not detected by any other characterization technique. The chemical state of the atoms on the surface of ZnO and the elemental composition were examined via XPS measurements. Figure 1B represents the XPS survey spectra of ZnO and Ti-ZnO. The well defined peaks centered at 1044, 1021, 531, 475, 459, 285, 140, 98 and 10 eV are ascribed to the binding energy of Zn2p_{1/2}, Zn2p_{3/2}, O1s, ZnLMM1, Ti2p, C1s, Zn3s, Zn3d and Zn3p respectively. The high-resolution spectra of Zn2p and Ti2P with different dopant consideration are shown in Figure 1C,D. The morphological changes and particle size of the synthesized ZnO

with controllable titanium doping concentration were observed by SEM measurements. The SEM images shown in Figure 2A,B prove that the prepared ZnO and Ti-ZnO samples were composed of nanoparticles with particle sizes of ca. 9–13 nm, while the incorporation of the doping particle did not induce any significant change in their morphology but decreased the particle size. The typical crystalline behavior, morphology and Ti ion distribution in the ZnO crystal lattice are further confirmed from TEM images depicted in Figure 2C,D. The corresponding TEM images reveal that the obtained materials were well crystallized, and the selected area electron diffraction (SAED) pattern inset in Figure 2C indicates ((101), (102) and (110)) a well-crystallized plane of ZnO. In addition, the lattice distance 0.24 nm shown in Figure 2D matches with the (101) plane ZnO crystal (slightly decrease of pure ZnO: 0.25 nm), indicating that Ti ions were evenly distributed in ZnO crystal lattice.

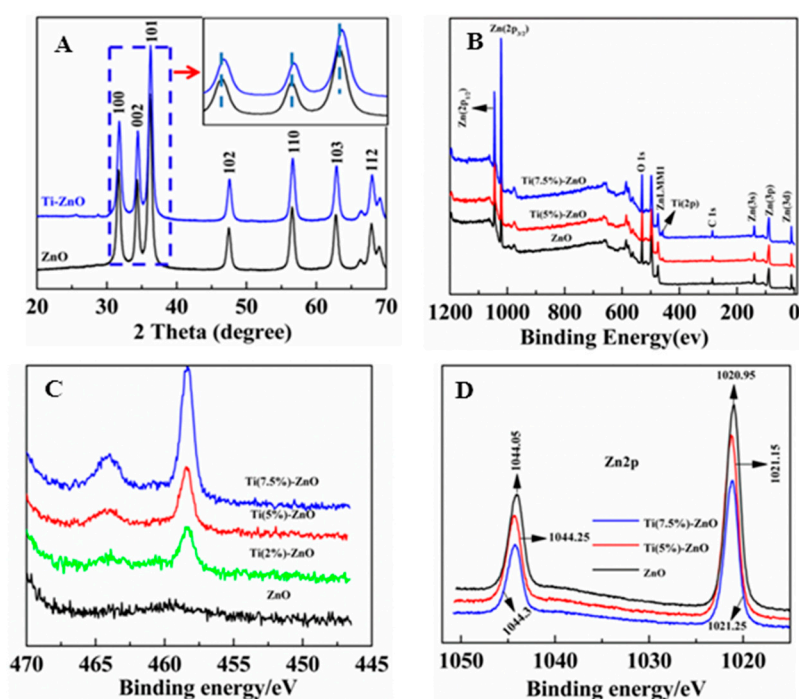


Figure 1. X-ray diffraction patterns of ZnO and Ti(7.5%)-ZnO, (A) XPS spectra of ZnO and Ti-ZnO, (B) survey spectra, (C) high-resolution spectra of Ti2p, and (D) Zn2p respectively.

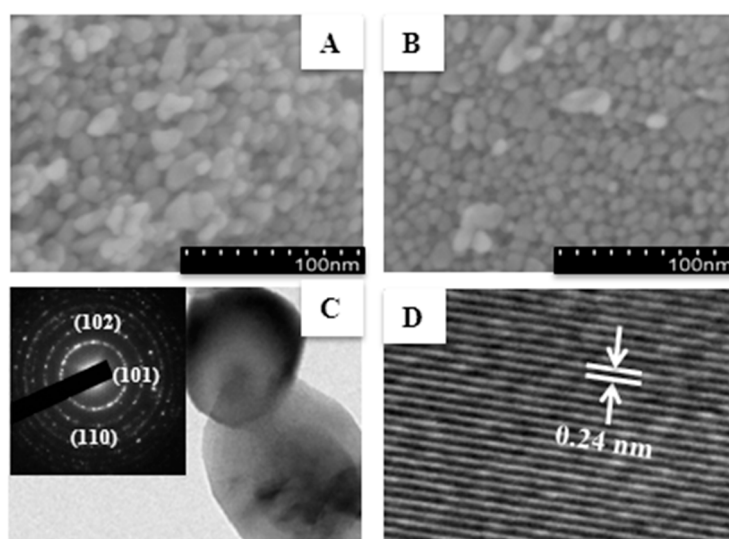


Figure 2. SEM images of (A) ZnO, (B) Ti-ZnO, (C) TEM, images of Ti-ZnO, and (D) HRTEM image of Ti-ZnO.

The surface area and pore size distribution of ZnO and Ti-ZnO nanoparticles were performed with Brunauer-Emmett-Teller (BET) by using N₂ adsorption-desorption isotherm. The XRD and BET results were in good alignment. From the results in Figure 3 and Table S1, it confirms that the surface area of (Ti-ZnO) under the same synthetic conditions dramatically increased from 45.38 to 131.85 m² g⁻¹ and the average pore size distribution of Ti-ZnO (3.4 nm) was slightly greater compared to ZnO (2.8 nm). The increment in BET surface area and pore size may be due to the inhibition of the ZnO crystallites growth with the incorporation of Ti dopant. The smaller size of Ti-ZnO would possess of higher BET surface area and larger pore size according to the small size effect of nanomaterials. The higher BET surface area and larger pore size would contribute to the higher dye loading, leading to enhanced light harvesting efficiency.

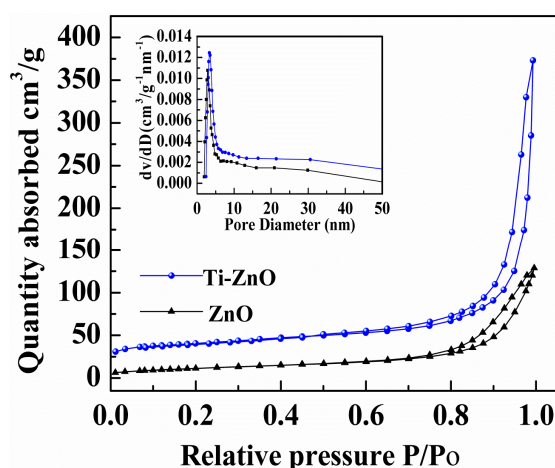


Figure 3. N₂ adsorption–desorption isotherms and pore size distribution (inset) of Ti-ZnO and ZnO nanoparticles.

The doped materials were further analyzed for elemental percentage of titanium in Ti-ZnO samples via ICP-OES, the data are summarized in Table 1. The ICP-OES analytical and EDS data are in best alignment with calculated values as observed from the ICP-OES analytical results and EDS spectra depicted in Figure S2.

Table 1. Elemental analysis of Ti percentage in Ti-ZnO samples.

S/No	Sample Name	Titanium (%)	
		Calculated	Observed
1	Ti(1%)-ZnO	1.0	0.96
2	Ti(2%)-ZnO	2.0	1.84
3	Ti(5%)-ZnO	5.0	4.71
4	Ti(7.5%)-ZnO	7.5	7.23

UV-visible characterization is a significant technique to assess the quantum confinement effects and band gap. In order to analyze the optical changes (effect of doping on the band gap), the UV absorption spectra were measured at room temperature in the range of 200 to 800 nm as displayed in Figure 4, the broad absorption band at 399 nm in ZnO was shifted to a higher wavelength of 426 nm with incorporation of Ti, which was assigned to the ligand-metal-charge transfer in the octahedral environment. After the successive incorporation of Ti, the resultant products showed more visible light absorbance (visible light utilizing efficiency) compared to pure ZnO, which might be attributable to the fact that the light scattering effect of ZnO was enhanced by Ti doping. Meanwhile, the decrease in bandgap, was well corresponded to the visible spectrum. The bandgap energy (E_g) was calculated from UV-visible spectrum using Equation (1).

$$E_g = 1240/\lambda \quad (1)$$

where λ is the wavelength measured from UV-visible absorption spectra Figure 4. The Ti-ZnO possesses a narrow forbidden E_g of 2.91 eV, is well corresponding to higher visible light harvesting efficiency, which is conducive to produce more photo-generated electrons and enhancement of short current density, as confirmed from IPCE measurement. The valence (VB) and conduction bands (CB) were estimated from oxidation potential (E_{ox}) by cyclic voltammetry (Figure S4) through equations in literature [36]. The corresponding results were manifested in Table S3. Based on optical and electrochemical properties comparison, the band positions of dye N719 and Ti-ZnO are in good alignment which is very important for charge separation. In the DSSC, the dye-sensitized dye adsorbs the photon under solar illumination at its interface, then separation of charge take place at the interface. Due to the well-aligned band positions for the charge separation, the photo-generated electrons can be quickly transferred from excited dye to the conduction band of Ti-ZnO, and the external circuit resulting in the photocurrent. The LUMO level of the N719 dye is higher than that of Ti-ZnO and ZnO, so for the electron transport has a single directional pathway.

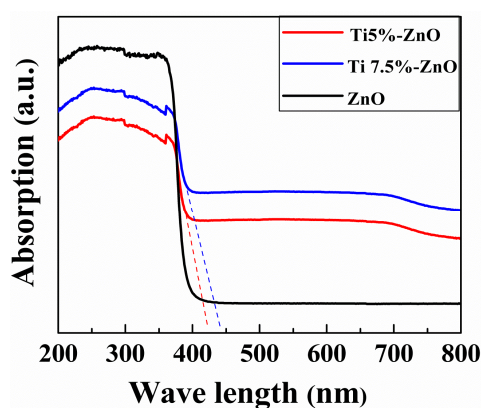


Figure 4. UV-Visible absorption spectra of the Ti(5%)-ZnO, Ti(7.5%)-ZnO and ZnO nanoparticles.

Raman spectroscopy is a sensitive technique for the analysis of subtle phase information, structural defects and crystallinity. ZnO has a hexagonal wurtzite structure with $C_{6v}P63mc$ space group, the group theory predicts that the Raman spectra of ZnO has two A_1 , two E_2 , two E_1 and two B_1 modes. To further study the crystallinity and effect of Ti in the framework structure of ZnO, both the Raman spectra of pure ZnO and Ti-ZnO were performed as shown in Figure 5. From the comparison of Raman spectra, it is evident that the well resolved peaks (TO, E_2 and LO phonon modes) small frequency shifting, broadening and intensity decrease in the Ti-ZnO sample might be ascribed to the disorder induced defects or oxygen vacancies and crystal lattice distortion [37].

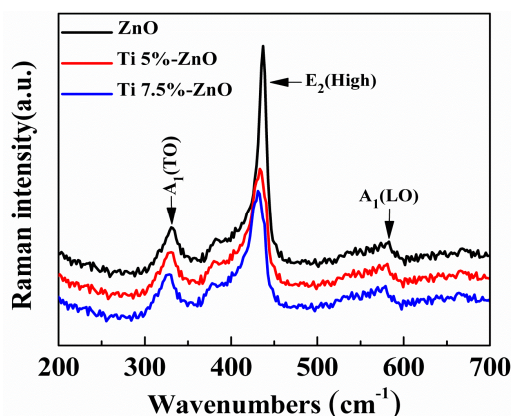


Figure 5. Raman spectra of the Ti(5%)-ZnO, Ti(7.5%)-ZnO and pure ZnO nanoparticles.

To determine the photovoltaic performance of ZnO and Ti-ZnO nanoparticles based DSSCs, three cells were fabricated for comparison. We have checked all the corresponding parameters which affect the power conversion efficiency of the devices like film thickness, dye immersion time, synthesis temperature and morphology of the materials etc. Finally three types of cells that showed high power conversion efficiencies, due to the quality of devices and photoanode films were investigated in this study. Cells were prepared with as synthesized ZnO, Ti(5%)-ZnO, and Ti(7.5%)-ZnO, respectively. The current-voltage curves are plotted in Figure 5 and the corresponding characteristic are summarized in Table 2. It can be observed that the cell composed of pure ZnO nanoparticles possessed a short-circuit current J_{sc} of 8.01 mA cm^{-2} and an efficiency of 3.82%. In comparison, higher J_{sc} and open-circuit voltage V_{oc} along with a PCE of 5.56% were obtained for the cell composed of Ti(7.5%)-ZnO. The increase in J_{sc} and V_{oc} might be attributed to improved light harvesting efficiency of the photoanode, compared with the highest PCE value of the cell composed of ZnO, the PCE was increased by 44.7%. As shown in Figure 6 both results (J_{sc} and IPCE) of the DSSCs based on ZnO, Ti(5%)-ZnO and Ti(7.5%)-ZnO are in good alignment with the results displayed in Table 2.

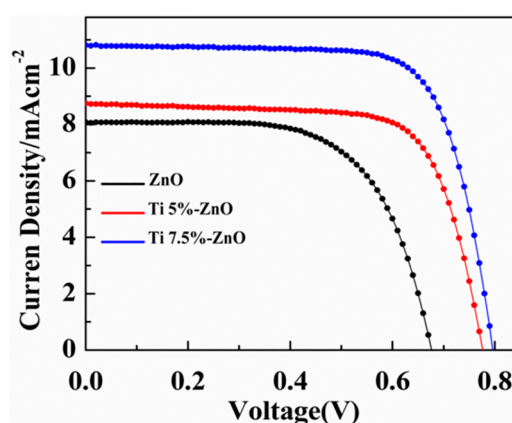


Figure 6. I-V curves of ZnO, Ti(5%)-ZnO and Ti(7.5%)-ZnO nanoparticles based DSSCs, in both the active area is 0.25 cm^2 and under (AM 1.5, 100 mW/cm^{-2}) illumination.

Table 2. Photovoltaic performance for the cells composed of ZnO and Ti-ZnO photoanodes

Cell	Photoanode	Thickness (μm)	J_{sc} (mA cm^{-2})	V_{oc} (V)	FF	η (%)	Dye Loading (10^{-7} mol/cm^2)
1	ZnO	10.9	8.01	0.68	0.64	3.82	1.10
2	Ti(5%)-ZnO	11.1	8.90	0.77	0.65	4.45	1.34
3	Ti(7.5%)-ZnO	11.2	10.92	0.79	0.64	5.56	1.85

All cells show the maximum incident-to-current conversion efficiency (IPCE) percentage at 550 nm wavelength corresponding to N719 dye adsorption peak as depicted in Figure 7. Furthermore, the adsorption amount of sensitizer dye directly influenced the quantum efficiency of the DSSCs. The IPCE peaks at 550 nm for Ti(7.5%)-ZnO is 73.76%, which is higher than 64.37% for Ti(5%)-ZnO and 57.23% for ZnO. In comparison the whole spectral region the Ti(7.5%)-ZnO showed considerable maximum IPCE value, which might be owing to the fact that Ti(7.5%)-ZnO, with a specific doping concentration of Ti, and narrow forbidden gap of E_g , increased the surface area and dye loading which directly influenced visible light absorbance and utilizing efficiency.

To support the photovoltaic performance enhancement and investigate the charge-transfer mechanism, the cells were analyzed via electrochemical impedance spectroscopy (EIS) under dark condition with -0.7 V applied voltage, their Nyquist plots are shown in Figure 8 and corresponding fitted results are summarized in Table 3. Two well-resolved semi-circles were observed in the measured frequency range. The R_s is ascribed to the photoanode film and FTO contact resistance. The small semicircle (R_{ct1}) that lies at high frequency range is described to transport resistance at the interface

of the counter electrode, while the large semicircle (R_{ct2}) at the low frequency range is charge recombination resistance at the interface of photoanode/electrolyte/dye. As observed from the EIS spectra of ZnO and Ti-ZnO cells, the R_{ct2} value increased with doping concentration indicating that the charge recombination resistance at the interface of ZnO/dye/electrolyte decreased remarkably.

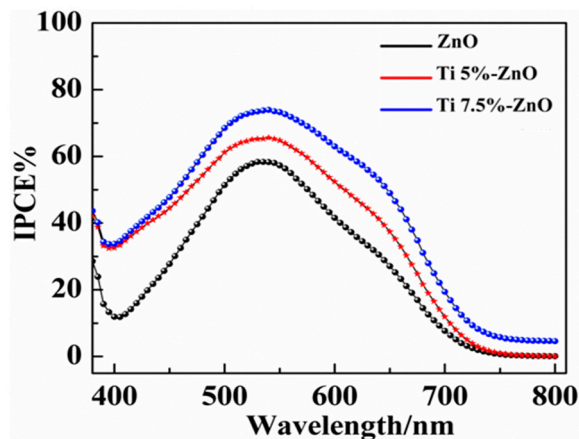


Figure 7. IPCE spectra of the ZnO, Ti(7.5%)-ZnO and Ti(5%)-ZnO nanoparticles based DSSCs.

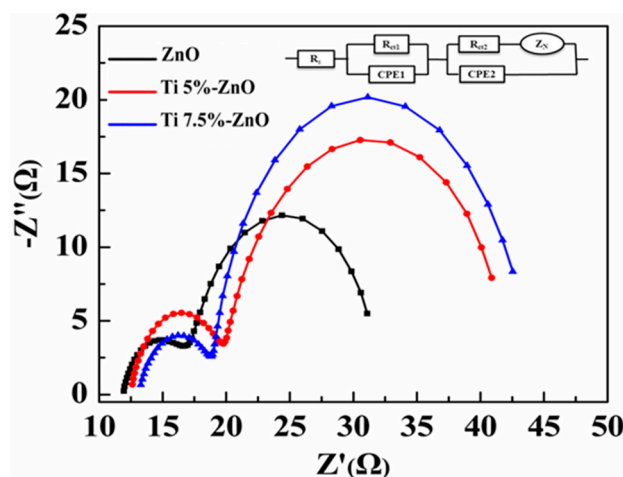


Figure 8. EIS spectra of the cells s composed of Ti(7.5%)-ZnO, Ti(5%)-ZnO and ZnO electrodes.

Table 3. EIS parameters of DSSCs based on ZnO and Ti-ZnO, with different dopant.

Cell	Working Electrode	R_s/Ω	R_{ct1}	$CPE1/F\text{ cm}^{-2}$	R_{ct2}/Ω	$CPE2/F\text{ cm}^{-2}$	$Z_N/\Omega\text{ cm}^{-2}$
1	ZnO	11.31	1.31	7.80×10^{-4}	31.2	4.35×10^{-4}	1.11×10^{-1}
2	Ti(5%)-ZnO	12.54	3.21	5.60×10^{-4}	43.5	2.09×10^{-3}	2.11×10^{-1}
3	Ti(7.5%)-ZnO	13.47	3.31	3.70×10^{-4}	46.4	5.25×10^{-4}	2.12×10^{-1}

Dye instability and carrier recombination in ZnO based DSSCs can occur across both the film–dye interface and film–electrolyte interface. Herein, we have discussed modifying the film/dye/electrolyte interface by way of Ti doping that is conformally doped into the oxide crystal lattice. It is well understood that the Ti doping can improve the ZnO based dye-sensitized solar cell efficiency by inhibiting the surface recombination of electrons at the film/dye/electrolyte interface by creating an energy barrier for physical separation of electrons. The dye and electrolyte stability of film significantly increases after Ti incorporation to the oxide crystal structure as shown in Figure S1B–D, fresh and stretched cells while the Figure S1A shows the cross section of the Ti-ZnO film. A photoanode with an increase in material surface area enhanced dye loading capability, which could be ascribed

from UV-visible adsorption spectra of devices, based on various surface area materials under the same film thickness, is shown in Figure 9. The photoanode composed of Ti(7.5%)-Zn has a large BET surface area and sufficient dye-loading capability of $1.85 \times 10^{-7} \text{ mol cm}^{-2}$, corresponding to their better light harvesting ability.

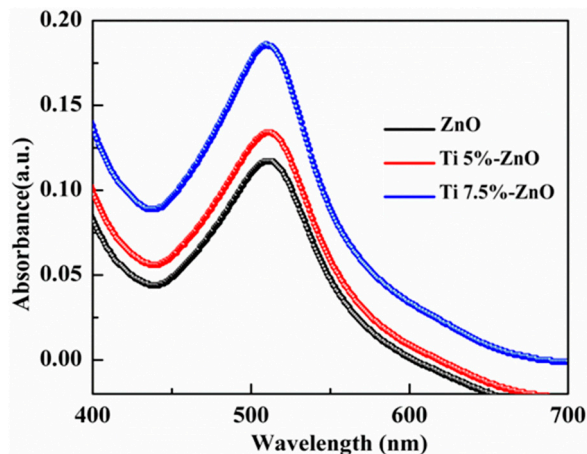


Figure 9. UV-Vis absorption spectra of DSSCs films based on ZnO and Ti(7.5%)-ZnO, Ti(5%)-ZnO.

4. Conclusions

In summary, Ti doped ZnO nanoparticles with mesoporous structure were synthesized via a simple synthetic route, and then successfully applied in dye-sensitized solar cells as a photoanode. It was found that ZnO nanoparticles decorated with Ti exhibited a superior light harvesting performance and the best efficiency of 5.56% could be obtained. Our experiments prove that the 44.7% photovoltaic performance enhancement can be possibly ascribed to the improved Fermi level and large surface area, which enhance dye loading ability, reduce charge recombination resistance and increase the harvest of photoexcited electrons. In conclusion the present work will provide a new route for the synthesis of efficient and unique working electrode materials.

Supplementary Materials: The following are available online at <http://www.mdpi.com/2073-4344/9/3/273/s1>, Figure S1: SEM images of ZnO and Ti doped ZnO, film thickness (A), ZnO stretched cell (B), Ti doped ZnO stretched and fresh cell (C, D), Figure S2: X-ray diffraction patterns of ZnO and Ti doped ZnO, with various percentage of Ti doping, Figure S3: EDX of TZ samples (1, 2, 3 and 4), Figure S4: CVs of (a) Ti-ZnO and (b) ZnO, Figure S5: X-ray diffraction pattern of Ti(10%)-ZnO, Table S1: Physiochemical properties of ZnO and TZ materials, Table S2: Elemental analysis of Ti percentage in TZ samples, Table S3: Optical and electrochemical properties of ZnO and Ti-ZnO.

Author Contributions: This research was a part of the PhD work of M.U.R. Under the supervision of M.W. The experimental work was carried out in Institute of Advanced Energy Materials, college of chemistry, Fuzhou University by M.U.R. under the supervision of M.W. M.U.R. wrote the manuscript, data analysis. F.X. and M.K. revised the manuscript. M.W. has done the technical supervision, and corresponding with journal for the manuscript.

Funding: This research received no external funding.

Acknowledgments: Qingqing Sun and Yafeng Li are acknowledged for their help with dye loading analysis.

Conflicts of Interest: The authors declare no conflict of interest.

References

- Grätzel, M. Solar Energy Conversion by Dye-Sensitized Photovoltaic Cells. *Inorg. Chem.* **2005**, *44*, 6841–6851. [[CrossRef](#)] [[PubMed](#)]
- Xiaoguang, M.; Swee Jen, C.; Benhu, F.; Jianyong, O. High-performance dye-sensitized solar cells with gel-coated binder-free carbon nanotube films as counter electrode. *Nanotechnology* **2010**, *21*, 395202.

3. Zhang, W.; Zhu, R.; Ke, L.; Liu, X.; Liu, B.; Ramakrishna, S. Anatase Mesoporous TiO₂ Nanofibers with High Surface Area for Solid-State Dye-Sensitized Solar Cells. *Small* **2010**, *6*, 2176–2182. [[CrossRef](#)] [[PubMed](#)]
4. Poudel, P.; Qiao, Q. One dimensional nanostructure/nanoparticle composites as photoanodes for dye-sensitized solar cells. *Nanoscale* **2012**, *4*, 2826–2838. [[CrossRef](#)]
5. Wu, M.; Lin, X.; Wang, T.; Qiu, J.; Ma, T. Low-cost dye-sensitized solar cell based on nine kinds of carbon counter electrodes. *Energy Environ. Sci.* **2011**, *4*, 2308–2315. [[CrossRef](#)]
6. Shao, F.; Sun, J.; Gao, L.; Yang, S.; Luo, J. Growth of Various TiO₂ Nanostructures for Dye-Sensitized Solar Cells. *J. Phys. Chem. C* **2011**, *115*, 1819–1823. [[CrossRef](#)]
7. O'Regan, B.; Gratzel, M. A low-cost, high-efficiency solar cell based on dye-sensitized colloidal TiO₂ films. *Nat.* **1991**, *353*, 737–740. [[CrossRef](#)]
8. Wang, P.; Zakeeruddin, S.M.; Moser, J.E.; Humphry-Baker, R.; Comte, P.; Aranyos, V.; Hagfeldt, A.; Nazeeruddin, M.K.; Grätzel, M. Stable New Sensitizer with Improved Light Harvesting for Nanocrystalline Dye-Sensitized Solar Cells. *Adv. Mater.* **2004**, *16*, 1806–1811. [[CrossRef](#)]
9. Hendry, E.; Koeberg, M.; O'Regan, B.; Bonn, M. Local Field Effects on Electron Transport in Nanostructured TiO₂ Revealed by Terahertz Spectroscopy. *Nano Lett.* **2006**, *6*, 755–759. [[CrossRef](#)] [[PubMed](#)]
10. Yella, A.; Lee, H.-W.; Tsao, H.N.; Yi, C.; Chandiran, A.K.; Nazeeruddin, M.K.; Diao, E.W.-G.; Yeh, C.-Y.; Zakeeruddin, S.M.; Grätzel, M. Porphyrin-Sensitized Solar Cells with Cobalt (II/III)-Based Redox Electrolyte Exceed 12 Percent Efficiency. *Science* **2011**, *334*, 629–634. [[CrossRef](#)]
11. Peng, M.; Cai, X.; Fu, Y.; Yu, X.; Liu, S.; Deng, B.; Hany, K.; Zou, D. Facial synthesis of SnO₂ nanoparticle film for efficient fiber-shaped dye-sensitized solar cells. *J. Power Sources* **2014**, *247*, 249–255. [[CrossRef](#)]
12. Song, H.; Lee, K.-H.; Jeong, H.; Um, S.H.; Han, G.-S.; Jung, H.S.; Jung, G.Y. A simple self-assembly route to single crystalline SnO₂ nanorod growth by oriented attachment for dye sensitized solar cells. *Nanoscale* **2013**, *5*, 1188–1194. [[CrossRef](#)]
13. Ramasamy, E.; Lee, J. Ordered Mesoporous SnO₂-Based Photoanodes for High-Performance Dye-Sensitized Solar Cells. *J. Phys. Chem. C* **2010**, *114*, 22032–22037. [[CrossRef](#)]
14. Bendall, J.S.; Etgar, L.; Tan, S.C.; Cai, N.; Wang, P.; Zakeeruddin, S.M.; Gratzel, M.; Welland, M.E. An efficient DSSC based on ZnO nanowire photo-anodes and a new D-[small pi]-A organic dye. *Energy Environ. Sci.* **2011**, *4*, 2903–2908. [[CrossRef](#)]
15. Xia, J.B.; Li, F.Y.; Yang, S.M.; Huang, C.H. Composite electrode SnO₂/TiO₂ for dye-sensitized solar cells. *Chin. Chem. Lett.* **2004**, *15*, 619–622.
16. Chen, S.G.; Chappel, S.; Diamant, Y.; Zaban, A. Preparation of Nb₂O₅ Coated TiO₂ Nanoporous Electrodes and Their Application in Dye-Sensitized Solar Cells. *Chem. Mater.* **2001**, *13*, 4629–4634. [[CrossRef](#)]
17. Gubbala, S.; Chakrapani, V.; Kumar, V.; Sunkara, M.K. Band-Edge Engineered Hybrid Structures for Dye-Sensitized Solar Cells Based on SnO₂ Nanowires. *Adv. Funct. Mater.* **2008**, *18*, 2411–2418. [[CrossRef](#)]
18. Prasittichai, C.; Hupp, J.T. Surface modification of SnO₂ photoelectrodes in dye-sensitized solar cells: Significant improvements in photovoltage via Al₂O₃ atomic layer deposition. *J. Phys. Chem. Lett.* **2010**, *1*, 1611–1615. [[CrossRef](#)]
19. Qian, J.; Liu, P.; Xiao, Y.; Jiang, Y.; Cao, Y.; Ai, X.; Yang, H. TiO₂-coated multilayered SnO₂ hollow microspheres for dye-sensitized solar cells. *Adv. Mater.* **2009**, *21*, 3663–3667. [[CrossRef](#)]
20. Law, M.; Greene, L.E.; Johnson, J.C.; Saykally, R.; Yang, P. Nanowire dye-sensitized solar cells. *Nat. Mater.* **2005**, *4*, 455–459. [[CrossRef](#)]
21. Archana, P.S.; Jose, R.; Vijila, C.; Ramakrishna, S. Improved Electron Diffusion Coefficient in Electrospun TiO₂ Nanowires. *J. Phys. Chem. C* **2009**, *113*, 21538–21542. [[CrossRef](#)]
22. Hosono, E.; Fujihara, S.; Kimura, T. Synthesis, structure and photoelectrochemical performance of micro/nano-textured ZnO/eosin Y electrodes. *Electrochim. Acta* **2004**, *49*, 2287–2293. [[CrossRef](#)]
23. Chen, M.; Wang, Y.; Song, L.; Gunawan, P.; Zhong, Z.; She, X.; Su, F. Urchin-like ZnO microspheres synthesized by thermal decomposition of hydrozincite as a copper catalyst promoter for the Rochow reaction. *RSC Adv.* **2012**, *2*, 4164–4168. [[CrossRef](#)]
24. Lin, L.; Yang, Y.; Men, L.; Wang, X.; He, D.; Chai, Y.; Zhao, B.; Ghoshroy, S.; Tang, Q. A highly efficient TiO₂@ZnO n-p-n heterojunction nanorod photocatalyst. *Nanoscale* **2013**, *5*, 588–593. [[CrossRef](#)]
25. Lee, D.; Rho, Y.; Allen, F.I.; Minor, A.M.; Ko, S.H.; Grigoropoulos, C.P. Synthesis of hierarchical TiO₂ nanowires with densely-packed and omnidirectional branches. *Nanoscale* **2013**, *5*, 11147–11152. [[CrossRef](#)]

26. Herman, I.; Yeo, J.; Hong, S.; Lee, D.; Nam, K.H.; Choi, J.-H.; Hong, W.-H.; Lee, D.; Grigoropoulos, C.P.; Ko, S.H. Hierarchical weeping willow nano-tree growth and effect of branching on dye-sensitized solar cell efficiency. *Nanotechnology* **2012**, *23*, 194005. [[CrossRef](#)]
27. Ko, S.H.; Lee, D.; Kang, H.W.; Nam, K.H.; Yeo, J.Y.; Hong, S.J.; Grigoropoulos, C.P.; Sung, H.J. Nanoforest of Hydrothermally Grown Hierarchical ZnO Nanowires for a High Efficiency Dye-Sensitized Solar Cell. *Nano Lett.* **2011**, *11*, 666–671. [[CrossRef](#)]
28. Yin, X.; Que, W.; Fei, D.; Xie, H.; He, Z.; Wang, G. Strategies to prepare an efficient photoanode for ZnO nanowires-based CdS–CdSe co-sensitized solar cells. *Electrochim. Acta* **2013**, *89*, 561–570. [[CrossRef](#)]
29. Keis, K.; Bauer, C.; Boschloo, G.; Hagfeldt, A.; Westermarck, K.; Rensmo, H.; Siegbahn, H. Nanostructured ZnO electrodes for dye-sensitized solar cell applications. *J. Photochem. Photobiol. A Chem.* **2002**, *148*, 57–64. [[CrossRef](#)]
30. Han, Z.; Ren, L.; Cui, Z.; Chen, C.; Pan, H.; Chen, J. Ag/ZnO flower heterostructures as a visible-light driven photocatalyst via surface plasmon resonance. *Appl. Catal. B: Environ.* **2012**, *126*, 298–305. [[CrossRef](#)]
31. Lee, S.-H.; Han, S.-H.; Jung, H.S.; Shin, H.; Lee, J.; Noh, J.-H.; Lee, S.; Cho, I.-S.; Lee, J.-K.; Kim, J.; et al. Al-Doped ZnO Thin Film: A New Transparent Conducting Layer for ZnO Nanowire-Based Dye-Sensitized Solar Cells. *J. Phys. Chem. C* **2010**, *114*, 7185–7189. [[CrossRef](#)]
32. Kao, C.H.; Wang, J.C.; Lai, C.S.; Huang, C.Y.; Ou, J.C.; Wang, H.Y. Ti-doped Gd₂O₃ sensing membrane for electrolyte–insulator–semiconductor pH sensor. *Thin Solid Films* **2012**, *520*, 3760–3763. [[CrossRef](#)]
33. Wei, M.; Wang, K.; Yanagida, M.; Sugihara, H.; Morris, M.A.; Holmes, J.D.; Zhou, H. Supercritical fluid processing of mesoporous crystalline TiO₂ thin films for highly efficient dye-sensitized solar cells. *J. Mater. Chem.* **2007**, *17*, 3888–3893. [[CrossRef](#)]
34. Pang, A.; Sun, X.; Ruan, H.; Li, Y.; Dai, S.; Wei, M. Highly efficient dye-sensitized solar cells composed of TiO₂@SnO₂ core–shell microspheres. *Nano Energy* **2014**, *5*, 82–90. [[CrossRef](#)]
35. Rahman, M.u.; Ullah Wazir, H.; Khan, M.; Nosheen, S.; Rahman, S.; Ullah, A. Precursor-Induced Template free hydrothermal synthesis of Faujasite and its Application in Catalytic Pyrolysis. *Mater. Res. Express* **2017**, *4*, 055009. [[CrossRef](#)]
36. Xiao, Y.; Han, G.; Wu, J.; Lin, J.-Y. Efficient bifacial perovskite solar cell based on a highly transparent poly(3,4-ethylenedioxythiophene) as the p-type hole-transporting material. *J. Power Sources* **2016**, *306*, 171–177. [[CrossRef](#)]
37. Acharya, S.A.; Maheshwari, N.; Tatikondewar, L.; Kshirsagar, A.; Kulkarni, S.K. Ethylenediamine-Mediated Wurtzite Phase Formation in ZnS. *Cryst. Growth Des.* **2013**, *13*, 1369–1376. [[CrossRef](#)]

